

iPEAR: Iterative Pyramid Estimation with Attention and Residuals for Deformable Medical Image Registration

Heming Wu¹ Di Wang² Tai Ma³ Peng Zhao⁴ Yubin Xiao⁴ Zhongke Wu⁵ Xing-Ce Wang⁵ Xuan Wu⁴
You Zhou^{1,4}

Abstract

Existing pyramid registration networks may accumulate anatomical misalignments and lack an effective mechanism to dynamically determine the number of optimization iterations under varying deformation requirements across images, leading to degraded performance. To solve these limitations, we propose **iPEAR**. Specifically, iPEAR adopts our proposed Fused Attention-Residual Module (FARM) for decoding, which comprises an attention pathway and a residual pathway to alleviate the accumulation of anatomical misalignment. We further propose a dual-stage Threshold-Controlled Iterative (TCI) strategy that adaptively determines the number of optimization iterations for varying images by evaluating registration stability and convergence. Extensive experiments on three public brain MRI datasets and one public abdomen CT dataset show that iPEAR outperforms state-of-the-art (SOTA) registration networks in terms of accuracy, while achieving on-par inference speed and model parameter size. Generalization and ablation studies further validate the effectiveness of the proposed FARM and TCI.

1. Introduction

In single-modality settings, deformable image registration aims to align the corresponding anatomical structures between a fixed and moving image pair within the same imaging modality by estimating a dense non-linear deformation field, with widespread real-world applications in medical

image analysis (Cai et al., 2020; Rana et al., 2019). To estimate the deformation field, conventional methods perform separate optimizations for each image pair, incurring high computational costs (Fischer & Modersitzki, 2008).

To improve efficiency, deep learning methods have been widely adopted for deformable image registration, with pioneering works (Balakrishnan et al., 2018; De Vos et al., 2019) mainly adopting U-Net and Cascaded frameworks to estimate deformation fields and warp moving images. U-Net networks typically predict a single deformation field at the output layer, which limits their ability to model large and complex deformations (Lv et al., 2022). Cascaded schemes address this issue by employing multiple subnetworks at different scales to progressively refine the deformation field, but they often re-extract features redundantly and underutilize previously encoded representations (Wang et al., 2024).

To minimize unnecessary feature extraction, recent studies have proposed pyramid models (Kang et al., 2022; Liu et al., 2022) that employ a single encoder to extract multi-scale feature maps. Subsequently, at each scale, the decoding layer fuses the feature maps extracted from both the fixed and moving image branches to estimate the deformation field. The estimated deformation field is then passed to the subsequent decoding layer (see Figure 1(a)), thereby achieving coarse-to-fine estimation. Although pyramid architectures facilitate multi-scale feature extraction, their decoders may exacerbate the propagation and accumulation of anatomical structure misalignments, especially those stemmed from irrelevant information in deep, coarse-scale features. This exacerbation ultimately constrains the overall registration performance (Zhou et al., 2023). In addition, existing single-modality pyramid models often adopt vanilla residual decoders, which limit their performance (see Tables 1 and 2). Moreover, in scenarios involving large deformations, a one-pass estimation per scale typically fails to yield an accurate deformation field, necessitating iterative estimations at each scale. Consequently, SOTA models perform multiple estimations at each scale to iteratively optimize the deformation fields. For example, Wang et al. (2024) adopted a fixed number of iterations, while Ma et al. (2024) introduced a single-stage mechanism to dynamically deter-

¹College of Software, Jilin University ²Joint NTU-UBC Research Centre of Excellence in Active Living for the Elderly, Nanyang Technological University ³College of Computer Science and Technology, Zhejiang University ⁴Key Laboratory of Symbolic Computation and Knowledge Engineering of Ministry of Education, College of Computer Science and Technology, Jilin University ⁵School of Artificial Intelligence, Beijing Normal University. Correspondence to: Xuan Wu <wuuu22@mails.jlu.edu.cn>, You Zhou <zyou@jlu.edu.cn>.

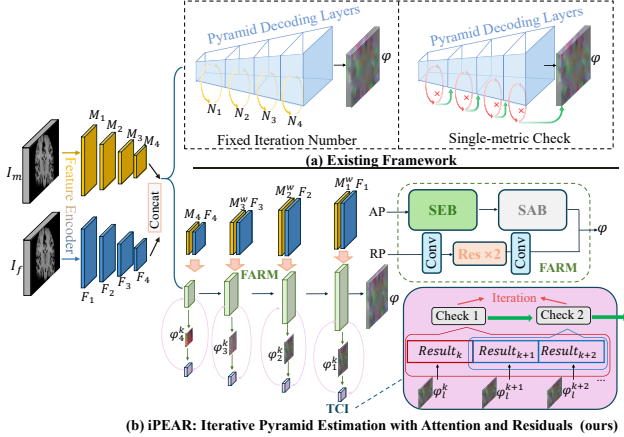


Figure 1. Illustration of the differences in decoding processes between existing pyramid models and our proposed iPEAR. Sub-figure (a) portrays the existing models (Wang et al., 2024) (left) and (Ma et al., 2024) (right), which do not specifically prevent propagation and accumulation of anatomical structure misalignments nor adaptively determine the number of iterations. Sub-figure (b) depicts our proposed iPEAR. At each decoding layer, iPEAR employs our designed FARM to learn to suppress irrelevant features, thereby reducing misalignment accumulation. Subsequently, iPEAR employs our novel dual-stage TCI strategy to adaptively determine the number of iterations for guiding FARM in the progressive optimization process of the deformation field.

mine the number of iterations at each scale. However, due to the diversity among image pairs, neither a fixed number of iterations nor a single-stage criterion may effectively adapt to varying deformation requirements, often resulting in premature termination or excessive iterations that degrade registration performance (see Section 4.1).

To mitigate misalignment propagation and accumulation in pyramid architectures, we propose the Fused Attention-Residual Module (**FARM**) as the core component of the decoding layer to emphasize informative features. Specifically, FARM follows a dual-pathway design, including an Attention Pathway (AP) and a Residual Pathway (RP) (see Figure 1 (b)). The AP comprises a Squeeze Excitation Block (SEB) and a Spatial Attention Block (SAB). SEB applies channel attention to suppress irrelevant features and alleviate accumulated anatomical misalignment, while SAB further highlights salient spatial regions based on the refined feature maps, thereby reducing misalignment accumulation. In parallel, RP employs two convolutional layers for channel transformation and two sequential residual blocks to extract fine-grained anatomical details, supporting comprehensive and precise structural modeling (see Section 3.1). By adopting this design, FARM achieves high-level registration performance compared to a vanilla residual decoder without substantially increasing the number of learnable parameters. Moreover, to adaptively determine the number of optimization iterations for diverse image pairs, we propose the dual-stage Threshold-Controlled Iterative (**TCI**) strategy, which employs a sliding window of size t to dynamically

track the estimated deformation fields and quantifies each by the similarity difference between the warped moving image I_m^w and the fixed image I_f . TCI then assesses the stability of deformation (i.e., first stage) by computing the standard deviation ε_l of all similarity differences within this window. Upon reaching stability (see Section 3.2), TCI further evaluates convergence (i.e., second stage) by measuring the change Δs between similarity differences of the two most recently estimated deformation fields within this window. TCI is designed to be efficient to enable adaptive determination of the number of iterations for each scale of the underlying image pair, without significantly increasing registration time (see Section 4.1). We coin the network that integrates FARM and TCI as the iterative Pyramid Estimation with Attention and Residuals (**iPEAR**) network. **To the best of our knowledge, iPEAR is the first pyramid network to jointly model channel and spatial attention alongside residual blocks in its decoder, while dynamically determining the number of optimization iterations.**

The key contributions of this work are as follows:

- I**) We propose a dual-pathway FARM for decoding, comprising AP and RP, where AP suppresses irrelevant information and RP extracts fine-grained anatomical details.
- II**) We propose the dual-stage TCI strategy, which monitors the stability and convergence of recent registration results to adaptively determine the number of optimization iterations for image pairs with varying deformation requirements.
- III**) To assess the performance of iPEAR, we conduct experiments on three public brain Magnetic Resonance Imaging (MRI) datasets spanning different deformation scales and one public abdomen Computed Tomography (CT) dataset. The experimental results demonstrate that iPEAR outperforms SOTA registration models in accuracy across all datasets, while achieving on-par inference speed and model parameter size. Moreover, generalization and ablation studies further validate the effectiveness of FARM and TCI.

2. Related Work

In this section, we review the relevant literature.

Deep Learning (DL) Registration Models: DL models have become the mainstream for solving registration tasks due to their advantages in inference speed and accuracy compared to conventional methods (Balakrishnan et al., 2019). Pioneer DL models primarily employed U-Net architectures, which estimate only a single deformation field at the final output layer and consequently struggle to accommodate complex deformations (Wang & Wang, 2025). To overcome this limitation, certain studies (De Vos et al., 2019; Zhao et al., 2019a;b) proposed cascaded registration networks, which employ multiple sub-networks to extract features at

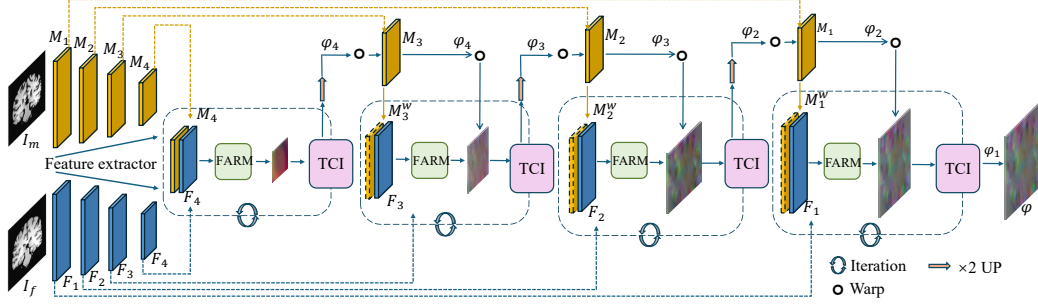


Figure 2. Overall iPEAR model architecture. A weight-sharing encoder first extracts multi-scale feature maps $\{F_l\}$ and $\{M_l\}$ for the fixed image I_f and the moving image I_m , respectively. In the subsequent decoding layers, iPEAR employs FARM to emphasize informative features and estimate the deformation field φ_l , while TCI adaptively determines the number of iterations for each decoding layer, enabling progressive optimization of φ_l . Notably, the encoder processes higher-resolution feature maps first ($F_1 \rightarrow F_4$, $M_1 \rightarrow M_4$), while the decoder begins deformation estimation on the lowest-resolution maps and proceeds to finer scales ($F_4 \rightarrow F_1$, $M_4 \rightarrow M_1$).

distinct resolutions and estimate the corresponding deformation fields. Although these models achieve moderate accuracy improvements, they perform repeated encoding and decoding, leading to redundant feature extraction and elevated computing overhead (Ma et al., 2024). To minimize redundant feature processing, recent studies (Liu et al., 2022) proposed the pyramid network, which adopts a single encoder followed by multiple decoding layers to estimate hierarchical deformation fields for continuous coarse-to-fine warping images. Although this architecture facilitates effective multi-scale feature extraction and progressive deformation estimation, it may exacerbate the propagation and accumulation of anatomical structure misalignments, especially those stemmed from irrelevant information in deep, coarse-scale features, ultimately affecting the overall registration performance (Zhou et al., 2023). To better overcome this limitation, we propose FARM to suppress irrelevant features in the decoding layers, thereby mitigating misalignment propagation. Moreover, FARM excels at capturing anatomical details, ensuring the accuracy and consistency of deformation fields at each scale (see Section 3.1).

Iterative Strategy in Pyramid Models: For small deformations, prior pyramid models (Kang et al., 2022) estimated only a single deformation field per decoding layer (each corresponding to one scale). However, under large deformations, a single estimation per scale is often insufficient to produce an accurate deformation field. Consequently, each scale requires iterative estimations to refine the deformation field. For example, Wang et al. (2024) proposed RDP, which performs a predefined number of iterations for each scale to refine the deformation field. Inevitably, this fixed number of iterations lacks adaptability to varying deformation requirements. To adaptively determine the number of iterations, Ma et al. (2024) proposed a single-stage mechanism, which evaluates convergence by monitoring differences between two successive registration results. However, relying on a single-metric check only captures partial information and may lead to premature iteration termination, potentially compromising the overall registration accuracy (see Tables 4

and F). To dynamically determine when to stop iterative optimization, we propose a dual-stage mechanism, which evaluates the stability of historical registration results and convergence subsequently (see Section 3.2 for more details).

3. iPEAR Dynamics

The architecture of **iPEAR** is schematically illustrated in Figure 2. In this section, we first introduce **FARM**, which extracts anatomical structure details and learns to suppress irrelevant features to mitigate misalignment. We then introduce the dual-stage **TCI** strategy, which adaptively determines the number of iterations for optimization.

Overview of iPEAR: iPEAR comprises a multi-scale encoder and a multi-layer decoder. iPEAR first employs a weight-sharing feature encoder to extract multi-scale feature map sets $\{F_l\}$ and $\{M_l\}$, where $l \in \{1, \dots, 4\}$ (following prior arts in this field: (Kang et al., 2022; Ma et al., 2024)), from the fixed image I_f and moving image I_m , respectively. Specifically, iPEAR adopts the encoder used in (Wang & Wang, 2025), which comprises four hierarchical convolutional encoder blocks. Each block includes a 3D convolutional layer followed by Neighborhood Attention (Hassani et al., 2023) (except for the first block), and then applies average pooling to halve the spatial dimensions of the feature maps. Then, for the l th scale (i.e., l th decoding layer), iPEAR applies FARM to process $\{F_l\}$ and $\{M_l\}$, extracting anatomical structure details and learning to suppress irrelevant features, to estimate the corresponding deformation fields (see Section 3.1). To adaptively determine the number of iterations in each decoding layer, iPEAR relies on TCI, which monitors the similarity difference of the recently estimated registration results (see Section 3.2).

3.1. Fused Attention-Residual Module (FARM)

Conventional residual convolutional structures, while effective at preserving anatomical consistency and modeling local details, typically apply uniform weighting across feature

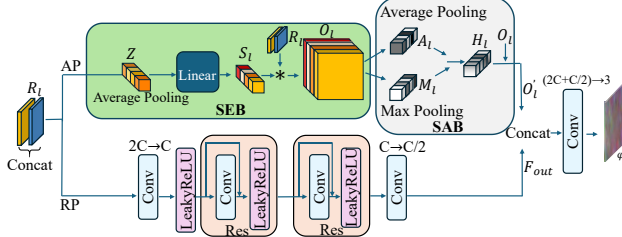


Figure 3. The proposed FARM adopts a dual-pathway architecture. The AP is composed of SEB and SAB. SEB applies channel attention to suppress irrelevant features and alleviate accumulated anatomical misalignment. Building on these refined feature maps, SAB emphasizes salient spatial regions, which further reduces misalignment accumulation. In parallel, RP includes two convolutional layers for channel transformation and two sequential residual blocks that extract fine-grained anatomical details, supporting comprehensive and precise structural modeling.

channels. This limits the network’s ability to emphasize subtle yet critical deformation cues that are essential for high-accuracy registration (Ma et al., 2024). In contrast, attention mechanisms excel at adaptively highlighting discriminative features and suppressing redundant information. However, when used alone, they often lack sufficient capability for robust local structure modeling and stable deformation estimation (Chen et al., 2022). Therefore, an effective decoder should combine the local modeling strength of residual convolutions with the adaptive feature selection of attention mechanisms to achieve high-level registration performance.

To this end, we propose FARM as the core component of the decoder for estimating deformation fields, which follows a dual-pathway design consisting of an Attention Pathway (AP) and a Residual Pathway (RP), as shown in Figure 3. Specifically, when $l = 4$ and $k = 1$, where k denotes the current iteration number at the l th layer, FARM directly takes F_4 and M_4 as inputs to estimate the deformation field $\varphi_4^1 \in \mathbb{R}^{C_\varphi \times H \times W \times D}$ via its dual-pathway architecture, where C_φ , H , W , and D denote the number of channels, height, width, and depth of the deformation field, respectively. When $l \in \{1, 2, 3\}$ and $k = 1$, FARM adopts the deformation field φ_{l+1} of the $(l+1)$ th layer to warp M_l to obtain M_l^w ($M_l^w = M_l \circ \varphi_{l+1}$), where \circ denotes the deformation operation, implemented via the Spatial Transformer Network (Jaderberg et al., 2015). Then, FARM utilizes F_l and M_l^w to estimate the deformation field $\varphi_l^1 \in \mathbb{R}^{C_\varphi \times H \times W \times D}$ for the l th layer through its dual pathways. Otherwise, FARM employs φ_l^{k-1} of the $(k-1)$ th iteration to warp M_l to obtain M_l^w ($M_l^w = M_l \circ \varphi_l^{k-1}$). Formally,

$$\varphi_l^k = \text{FARM}(R_l), \quad (1)$$

$$R_l = \begin{cases} (|M_4, F_4|), & l = 4 \wedge k = 1, \\ (|M_l^w, F_l|), & \text{Otherwise,} \end{cases} \quad (2)$$

where $|\cdot|$ denotes the concatenation operator, and the final expression of φ_l^k is given later in (13).

AP consists of a Squeeze-and-Excitation Block (SEB) and

a Spatial Attention Block (SAB), while RP comprises two convolutional layers for channel transformation and two sequential residual blocks. Specifically, AP extends the 2D SEB (Hu et al., 2018) to a 3D variant to suppress irrelevant features in R_l , thereby mitigating propagation and accumulation of anatomical misalignment. The 3D SEB first employs average pooling to compress spatial dimensions and extract global informative features, producing the channel descriptor vector $Z_l \in \mathbb{R}^{2C}$ as follows:

$$Z_{l,c} = \frac{1}{H \cdot W \cdot D} \sum_{i=1}^H \sum_{j=1}^W \sum_{d=1}^D R_{l,c,i,j,d}, \quad (3)$$

where C denotes the number of channels of the image and $c \in \{1, \dots, 2C\}$. Then, SEB applies two fully connected layers with LeakyReLU γ and sigmoid σ activation functions to compute the channel weight vector S_l as follows:

$$S_l = \sigma(W_2 \gamma(W_1 Z_l)), \quad (4)$$

where $W_1 \in \mathbb{R}^{\frac{2C}{r} \times 2C}$ and $W_2 \in \mathbb{R}^{2C \times \frac{2C}{r}}$. The hyper-parameter r denotes the reduction ratio, which is used to gauge the computational cost. The first linear layer reduces the dimensionality of Z_l to $\frac{2C}{r}$, for efficient channel-wise compression and information aggregation. The second linear layer then restores the dimensionality back to $2C$. By adopting this design, SEB can model inter-channel dependencies and recalibrate channel responses. Consequently, SEB adaptively emphasizes deformation-sensitive channels while suppressing less informative ones, mitigating the tendency of uniform channel weighting to overlook subtle yet critical deformation cues (see Table 5). Subsequently, the resulting weight vector S_l is applied to R_l via per-channel element-wise multiplication $*$, yielding the enhanced feature map $O_l \in \mathbb{R}^{2C \times H \times W \times D}$ as follows:

$$O_{l,c} = R_{l,c} * S_{l,c}, c \in \{1, \dots, 2C\}. \quad (5)$$

To further alleviate misalignment accumulation, SAB applies average pooling and max pooling to the enhanced feature map O_l to obtain descriptor vectors A_l and M_l , respectively. These two descriptors are then fused through a convolutional layer to produce the hybrid vector H_l , which captures complementary spatial cues. Formally,

$$H_l = \text{Conv}(|A_l, M_l|), \quad (6)$$

$$A_{l,c} = \frac{1}{H \cdot W \cdot D} \sum_{i=1}^H \sum_{j=1}^W \sum_{d=1}^D O_{l,c,i,j,d}, \quad (7)$$

$$M_{l,c} = \max_{i=\{1, \dots, H\}, j=\{1, \dots, W\}, d=\{1, \dots, D\}} O_{l,c,i,j,d}. \quad (8)$$

Subsequently, the descriptor vector H_l is applied to O_l via per-channel element-wise multiplication $*$, yielding the hybrid feature map $O'_l \in \mathbb{R}^{2C \times H \times W \times D}$ as follows:

$$O'_{l,c} = O_{l,c} * H_{l,c}, c \in \{1, \dots, 2C\}. \quad (9)$$

RP comprises a 3D convolutional layer Cl_1 , two residual blocks (Res_1 and Res_2), and a final 3D convolutional layer Cl_2 . Specifically, R_l is first fed into a 3D convolutional layer, which adjusts the channel dimension from $2C$ to C , followed by a LeakyReLU function γ . The resulting features then pass through Res_1 and Res_2 , each consisting of a 3D convolutional layer followed by γ . Finally, Cl_2 outputs the feature map F_{out} with $\frac{C}{2}$ channels. Formally,

$$Res_i(x) = \gamma(Conv(x) + x), i \in \{1, 2\}, \quad (10)$$

$$F_o = Cl_2^{C \rightarrow \frac{C}{2}}(Res_2(Res_1(\gamma(Cl_1^{2C \rightarrow C}(R_l)))), \quad (11)$$

where x denotes the input to the residual block. After obtaining O'_l and F_o , FARM finally applies a convolutional layer Cl_3 to combine them and estimate the intermediate deformation field $\bar{\varphi}_l^k$ for the k th iteration as follows:

$$\bar{\varphi}_l^k = Cl_3^{(\frac{C}{2} + 2C \rightarrow 3)}(|O'_l, F_o|). \quad (12)$$

After obtaining $\bar{\varphi}_l^k$, FARM forms the final φ_l^k for the k th iteration by composing it with the deformation field φ_l^{k-1} of the preceding iteration when $k \neq 1$. For the first iteration (i.e., $k = 1$) with $l \neq 4$, FARM uses the final deformation field from the $(l+1)$ th layer φ_{l+1} , in place of φ_l^{k-1} . When $l = 4$ and $k = 1$, FARM simply sets $\varphi_l^k = \bar{\varphi}_l^k$. Formally,

$$\varphi_l^k = \begin{cases} \varphi_l^{k-1} \circ \bar{\varphi}_l^k + \bar{\varphi}_l^k, & k \neq 1, \\ \varphi_{l+1} \circ \bar{\varphi}_l^k + \bar{\varphi}_l^k, & k = 1, l \neq 4, \\ \bar{\varphi}_l^k, & \text{Otherwise.} \end{cases} \quad (13)$$

Finally, when TCI terminates at the k th iteration, FARM upsamples φ_l^k with a factor of 2 to obtain the final deformation φ_l for the l th layer. Notably, unlike the decoder adopted by IIRP (Ma et al., 2024), which relies solely on multiple sequential residual blocks to estimate the deformation field, FARM integrates channel and spatial attention in parallel with a small number of residual blocks, designed to achieve enhanced performance through richer features (see Table 1). In addition, the results further validate that AP and RP effectively suppress irrelevant features and capture fine-grained anatomical details, respectively (see Appendix B for visualizations of feature attention patterns in AP and RP).

3.2. Threshold-Controlled Iterative (TCI) Strategy

The number of iterations is crucial for optimizing the deformation field; early termination may yield suboptimal accuracy, while excessive iterations may introduce misalignment and consume unnecessary computing resources. To adaptively determine the number of iterations for varying image pairs, we propose a dual-stage TCI strategy to evaluate both stability and convergence using historical registration results to dynamically determine when to stop. As shown in Figure 4, at the l th decoding layer, TCI employs a sliding

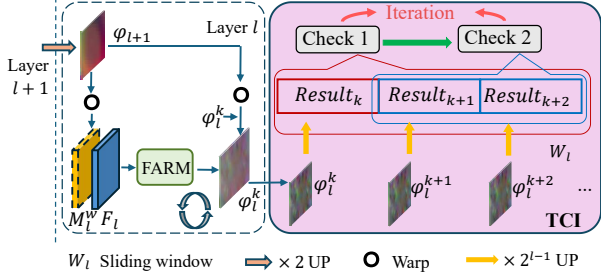


Figure 4. Depiction of the proposed TCI strategy, which determines when to stop the iteration through a dual-stage mechanism. TCI first checks whether the $\text{std } \varepsilon_l$ of similarity differences across all historical registration results in W_l is lower than a threshold δ_s . If yes, TCI further computes the change Δs between similarity differences of the two most recent registration results in W_l . If Δs is smaller than another threshold δ_c , it is considered that the appropriate stopping criteria have been reached.

window W_l to dynamically track the similarity differences of t number of recently estimated registration results.

To compute the similarity difference s_l^k between the warped image I_m^w and the fixed image I_f at the k th iteration, TCI first upsamples the deformation field φ_l^k , yielding the upsampled deformation field $\tilde{\varphi}_l^k$ at the original moving image resolution. The upsampling is implemented via linear interpolation with a factor of 2^{l-1} . Next, $\tilde{\varphi}_l^k$ provides a displacement vector for each voxel to be applied to the moving image I_m to produce the corresponding warped image I_m^w , i.e., $I_m^w = I_m \circ \tilde{\varphi}_l^k$. Formally,

$$s_l^k = \text{sim}(I_f, I_m^w), \quad (14)$$

where $\text{sim}(\cdot)$ denotes the similarity metric. In this work, we always adopt Normalized Cross-Correlation (NCC) to compute the registration similarity after examining various candidates (see Appendix I).

After obtaining the similarity differences of t number of recently estimated registration results, TCI evaluates their stability and convergence in a dual-stage process, respectively. In the first stage, TCI assesses stability by computing the standard deviation ε_l of similarity differences s_l^k within the window $W_l = \{s_l^{k-t+1}, \dots, s_l^k\}$ as follows:

$$\varepsilon_l = \text{std}(W_l). \quad (15)$$

If ε_l falls below the predefined stability threshold δ_s , the most recent t number of deformation fields are deemed stable. TCI then proceeds to the subsequent convergence evaluation stage. Otherwise, another iteration is performed without the necessity to continue the subsequent stage.

In the subsequent convergence evaluation stage, TCI further computes the change in similarity differences, denoted as Δs , between the two most recent iterations within W_l , which is defined as follows:

$$\Delta s = s_l^k - s_l^{k-1}. \quad (16)$$

Algorithm 1 Registration process in the l th decoding layer

```

1: Input: ( $l + 1$ )th deformation field  $\varphi_{l+1}$ , feature maps
    $F_l, M_l$ , original images  $I_f, I_m, W_l, k \leftarrow 1$ 
2: Output:  $l$ th deformation field  $\varphi_l$ 
3:  $\varphi_l^{k-1} \leftarrow \varphi_{l+1}$  #If  $k \neq 1 \vee l = 4$ , this step is skipped
4: while  $k \leq k_{max}$  do
5:    $M_l^w \leftarrow M_l \circ \varphi_l^{k-1}$  #If  $k = 1 \wedge l = 4$ , this step is skipped
6:    $R_l \leftarrow (|M_l^w, F_l|)$  #If  $k = 1 \wedge l = 4$ ,  $R_4 \leftarrow (|M_4, F_4|)$ 
7:    $O_l \leftarrow \mathbf{SEB}(R_l), H_l = \mathbf{SAB}(|O_l|)$ 
8:    $O_l' \leftarrow O_l * H_l$  #AP output
9:    $F_o \leftarrow Cl_2(Res_2(Res_1(\gamma(Cl_1(R_l)))))$  #RP output
10:   $\bar{\varphi}_l^k = Cl_3(|O_l', F_o|)$  #deformation estimation
11:   $\varphi_l^k \leftarrow \varphi_l^{k-1} \circ \bar{\varphi}_l^k + \bar{\varphi}_l^k$  #If  $l = 4 \wedge k = 1$ , this step
    is skipped.
12:   $\tilde{\varphi}_l^k \leftarrow \text{upsample}(\varphi_l^k, 2^{l-1})$ 
13:   $s_l^k \leftarrow \text{sim}(I_f, I_m \circ \tilde{\varphi}_l^k)$  #see (14)
14:  append  $s_l^k$  to  $W_l$  #If  $\text{len}(W_l) = t + 1$ , remove  $s_l^{k-t}$ 
    from  $W_l$ 
15:  if  $\text{len}(W_l) \geq t$  then #TCI invoked
16:     $\varepsilon_l \leftarrow \text{std}(W_l)$  #see (15)
17:    if  $\varepsilon_l \leq \delta_s$  then #Stage 1: assess stability
18:       $\Delta s \leftarrow s_l^k - s_l^{k-1}$  #see (16)
19:      if  $\Delta s \leq \delta_c$  then #Stage 2: assess convergence
20:        return  $\varphi_l \leftarrow \text{upsample}(\varphi_l^k, 2)$ 
21:     $k \leftarrow k + 1$ 
22:  end while
23: return  $\varphi_l \leftarrow \text{upsample}(\varphi_l^{k_{max}}, 2)$ 

```

If Δs falls below the predefined convergence threshold δ_c , the deformation field at the k th iteration is deemed converged, the iteration terminates and the deformation field φ_l is passed to the $(l - 1)$ th layer as input (see Figure 2). Otherwise, additional iterations continue at the l th layer. Following (Ma et al., 2024), TCI also leverages a predefined maximum number of iterations k_{max} to avoid rare non-convergence situations. The pseudocode of the overall registration process is presented in Algorithm 1.

Notably, our TCI fundamentally differs from IIRP’s single-stage method (Ma et al., 2024), which performs only one similarity check between two consecutive registrations and may prematurely terminate due to stochastic convergence. TCI adopts a two-stage evaluation with an additional stability check, enabling more informed stopping decisions while maintaining comparable inference time (see Table 4).

3.3. Loss Functions

Being an unsupervised registration network, similar to the prior SOTA model (Ma et al., 2024), iPEAR employs NCC to evaluate the loss between the fixed image I_f and the

warped moving image I_w^m , which is defined as follows:

$$\mathcal{L}_{ncc}(I_f, I_m^w) = - \sum_{p \in \Omega} \frac{\sum_{p_i} (I_f(p_i) - \bar{I}_f(p)) \cdot (I_m^w(p_i) - \bar{I}_m^w(p))}{\sqrt{\sum_{p_i} (I_f(p_i) - \bar{I}_f(p))^2 \cdot \sum_{p_i} (I_m^w(p_i) - \bar{I}_m^w(p))^2}}, \quad (17)$$

where Ω denotes the entire volume domain (i.e., the set of all voxels of the fixed image), p_i denotes the i th voxel within p ’s local neighborhood (i.e., the cubic patch of size n^3 centered at p), $\bar{I}_f(p)$ and $\bar{I}_m^w(p)$ denote the averaged voxel value of $I_f(p)$ and $I_m^w(p)$, respectively, computed over the corresponding neighborhoods.

Moreover, to enforce the smoothness of the deformation field, we incorporate the L_2 -norm $\|\cdot\|$ on the gradient of φ :

$$\mathcal{L}_{smooth}(\varphi) = \sum_{p \in \Omega} \|\nabla \varphi(p)\|^2. \quad (18)$$

Therefore, the total loss in iPEAR is defined as follows:

$$\mathcal{L}_{total}(I_f, I_m) = \mathcal{L}_{ncc}(I_f, I_m^w) + \lambda \mathcal{L}_{smooth}(\varphi), \quad (19)$$

where λ denotes the hyperparameter used to leverage relative importance in the overall loss function.

4. Experimental Results

To assess the performance of iPEAR, we conduct extensive experiments on three public MRI datasets, namely Mindboggle (Klein & Tourville, 2012), LPBA (Shattuck et al., 2008), and IXI (Avants et al., 2009), and one public abdomen CT dataset FLARE (Ma et al., 2022). While the SOTA models (Ma et al., 2024), (Cheng et al., 2025), and (Wang & Wang, 2025) were evaluated using two or three datasets, ours is more extensively evaluated. Appendix A describes these datasets, evaluation metrics, and experimental setups. The source code of iPEAR is available online anonymously¹.

4.1. Comparison against Baseline Models

To benchmark the performance of iPEAR, we choose two U-Net models, namely VM (Balakrishnan et al., 2019) and TM (Chen et al., 2022), two cascaded models, namely RCN (Zhao et al., 2019a) and SDH (Zhou et al., 2023), and eight multi-scale pyramid models, namely RDN (Hu et al., 2022), PR++ (Kang et al., 2022), I2G (Liu et al., 2022), PIVIT (Ma et al., 2023), RDP (Wang et al., 2024), IIRP (Ma et al., 2024), SACB (Cheng et al., 2025), and NAP (Wang & Wang, 2025) as baseline models. For these baselines, we evaluate them using the same data preprocessing pipeline as iPEAR to ensure a fair comparison. To account for randomness, we evaluate each model three times with different random seeds on each dataset and report the averaged results. Unfortunately, we are not able to include certain recent baseline models (ReCorr (Li et al., 2025) and RDMR (Hu et al., 2025)) due

¹<https://anonymous.4open.science/r/iPEAR>

Table 1. Performance comparison of different registration models on the Mindboggle, LPBA, and IXI datasets

Model	Mindboggle			LPBA			IXI			#Param. \downarrow	
	Dice(%) \uparrow	Time(s) \downarrow	$ J_\varphi _{\leq 0} \downarrow$	Dice(%) \uparrow	Time(s) \downarrow	$ J_\varphi _{\leq 0} \downarrow$	Dice(%) \uparrow	Time(s) \downarrow	$ J_\varphi _{\leq 0} \downarrow$		
Cascaded U-Net	VM (CVPR'18)	56.0	0.09	$<0.7\%$	65.1	0.02	$<0.3\%$	75.9	0.01	$<0.2\%$	319.4K
	TM (MIA'22)	61.5	0.10	$<1.0\%$	67.0	0.10	$<0.78\%$	76.9	0.03	$<0.43\%$	45650.3K
Pyramid	RCN (ICCV'19)	63.4	0.19	$<0.8\%$	71.4	0.05	$<0.007\%$	78.6	0.06	$<0.01\%$	958.1K
	SDH (TMI'23)	63.6	0.82	$<0.2\%$	70.5	0.77	$<0.4\%$	79.3	0.08	$<0.2\%$	17862.0K
PiViT (MICCAI'23)	RDN (JBHI'22)	62.5	0.08	$<0.03\%$	70.6	0.04	$<0.05\%$	78.8	0.02	$<0.06\%$	28653.2K
	PR++ (MIA'22)	63.1	0.47	$<0.5\%$	70.4	0.64	$<0.07\%$	79.3	0.07	$<0.06\%$	1208.0K
I2G (MMMI'22)	I2G (MMMI'22)	62.5	0.51	$<0.03\%$	71.7	0.06	$<0.006\%$	79.3	0.51	$<0.02\%$	865.2K
	PiViT (MICCAI'23)	64.1	0.46	$<0.03\%$	71.2	0.18	$<0.01\%$	79.7	0.48	$<0.02\%$	664.8K
IIRP (CVPR'24)	RDP (TMI'24)	65.5	0.37	<0.003%	73.1	0.26	<0.0002%	80.4	0.11	<0.003%	8922.4K
	IIRP (CVPR'24)	65.8	0.12	$<0.006\%$	72.2	0.10	$<0.02\%$	80.4	0.09	$<0.02\%$	410.1K
SACB (CVPR'25)	SACB (CVPR'25)	65.1	2.08	$<0.06\%$	73.1	1.45	$<0.02\%$	80.3	1.02	$<0.03\%$	1105.6K
	NAP (BSPC'25)	66.8	0.30	$<0.2\%$	73.7	0.28	$<0.03\%$	80.4	0.22	$<0.07\%$	501.9K
iPEAR (ours)	67.9	0.19	$<0.009\%$	73.7	0.15	$<0.003\%$	80.6	0.12	$<0.008\%$	508.7K	

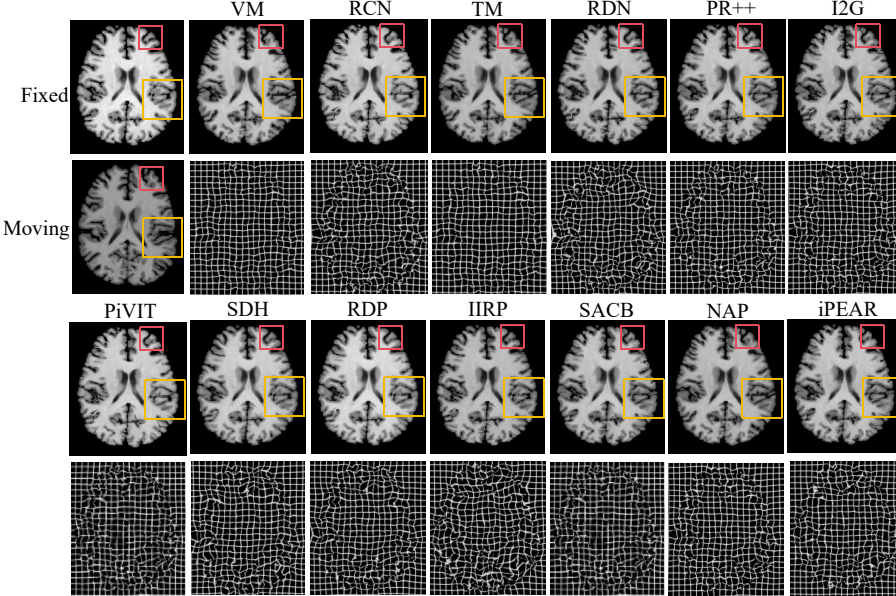


Figure 5. Visualization of registration results and corresponding deformation fields across different models on the Mindboggle dataset.

Table 2. Performance comparison on the FLARE dataset

Model	Dice(%) \uparrow	Time(s) \downarrow	$ J_\varphi _{\leq 0} \downarrow$
PR++ (MIA'22)	60.2	0.07	$<1.4\%$
RDP (TMI'24)	73.0	0.08	<0.03%
IIRP (CVPR'24)	73.8	0.03	$<2.0\%$
SACB (CVPR'25)	74.3	0.13	$<0.7\%$
NAP (BSPC'25)	74.9	0.16	$<2.0\%$
iPEAR (ours)	76.9	0.16	$<2.0\%$

to the incompleteness of the released source code. Table 1 presents the performance of different registration models on the Mindboggle, LPBA, and IXI datasets, measured using the Dice (Dice, 1945), Jacobian determinant ($|J_\varphi|_{\leq 0}$), and inference time (s) metrics. Appendix C presents HD95 (Huttenlocher et al., 1993), ASSD (Taha & Hanbury, 2015), and MSE metrics for these registration models across all three datasets. Table 2 presents the performance of different registration models (competing pyramid models in Table 1) on the FLARE dataset. The results shown in both tables

demonstrate that iPEAR outperforms all the other registration models on the Dice metric across all four datasets, with particularly strong gains on Mindboggle, a well-known challenging benchmark with large spatial displacements. These gains are largely attributed to FARM, which mitigates the limitation of conventional residual convolutional decoders that are widely adopted by existing models (e.g., SACB). Such decoders treat feature channels uniformly and may miss subtle but critical deformation cues. Equipped with FARM, iPEAR produces more accurate and robust deformation estimates by emphasizing informative features and suppressing irrelevant ones. Furthermore, FARM is lightweight, enabling iPEAR to achieve superior performance with only a modest increase in parameter size (approximately 1.2 \times) over IIRP. Consequently, the inference time does not increase substantially. Unlike SACB, which estimates the deformation field only once per decoding layer, iPEAR employs TCI to adaptively determine the number of iterations

Table 3. The generalizability of FARM on the IXI dataset

Model	Dice(%) \uparrow	MSE(10^{-3}) \downarrow
I2G (+ FARM)	79.3 (79.9)	0.40 (0.37)
PR++ (+ FARM)	79.3 (79.4)	0.36 (0.32)
IIRP (+ FARM)	80.4 (80.5)	0.24 (0.20)

Table 4. The generalizability of TCI

	Mindboggle			LPBA		
	Dice(%)	MSE \downarrow	Time(s) \downarrow	Dice(%)	MSE \downarrow	Time(s) \downarrow
IIRP	65.8	4.16	0.12	72.2	0.62	0.10
IIRP+TCI	66.2	3.56	0.14	73.0	0.61	0.14

at each layer, thereby yielding superior performance, achieving Dice improvements of 2.8%, 0.6%, 0.3%, and 2.6% on the four datasets, respectively. Notably, RDP and IIRP also employ iterative strategies. However, RDP adopts a fixed number of iterations and IIRP relies on a single-stage stopping criterion evaluation, both of which lead to inferior performance. In contrast, our iPEAR employs TCI with a dual-stage strategy at each decoding layer, thereby achieving elevated performance while incurring only a marginal increase in inference time over IIRP.

Figure 5 and Appendix D visualize the registration results on the Mindboggle and LPBA datasets, respectively. On Mindboggle, performance differences among models are more noticeable in the two structural regions of the brain images, highlighted using the red and yellow boxes. These visualizations further demonstrate that the moving images, after being warped by the deformation fields produced by iPEAR, align more closely with fixed images. Additionally, we perform quantitative analyses of specific regions in the left and right hemispheres to further illustrate variations in anatomical structure registration performance across different models. The results, as presented in Appendix E, further demonstrate the superior performance of iPEAR.

4.2. Generalizability of FARM and TCI

To demonstrate the generalizability of FARM and TCI, we integrate each into existing registration models and report the results in Tables 3 and 4, respectively. Table 3 shows that replacing the decoder with FARM yields consistent performance gains across all three pyramid models. This is because FARM adaptively emphasizes anatomically relevant features while suppressing less informative ones, thereby mitigating error accumulation during coarse-to-fine decoding. Furthermore, Table 4 demonstrates that substituting IIRP’s original single-stage iterative strategy with TCI yields performance improvement, underscoring the advantage of TCI in determining the number of optimization iterations dynamically. To provide in-depth details of this gain, we present the number of iterations determined by TCI and by the single-stage strategy across the four decoding levels of

Table 5. Ablation study on different FARM modules

SEB	SAB	RP	Mindboggle		LPBA		IXI	
			Dice(%) \uparrow	MSE \downarrow	Dice(%) \uparrow	MSE \downarrow	Dice(%) \uparrow	MSE \downarrow
\times	\times	\times	65.3	4.16	72.4	0.79	80.1	0.26
\times	\times	\checkmark	65.8	4.10	72.5	0.73	80.3	0.24
\checkmark	\times	\checkmark	66.2	4.02	73.4	0.71	80.4	0.24
\times	\checkmark	\checkmark	66.1	4.00	73.3	0.68	80.3	0.24
\checkmark	\checkmark	\times	67.5	3.98	73.5	0.65	80.4	0.23
\checkmark	\checkmark	\checkmark	67.9	3.97	73.7	0.61	80.6	0.23

Table 6. Ablation study on different TCI configurations

	TCI-1	TCI-2	TCI-3	TCI-4
Dice(%) \uparrow	80.4	80.4	80.5	80.6
MSE(10^{-3}) \downarrow	0.232	0.248	0.231	0.231

IIRP in Appendix F. Overall, these results indicate that TCI can alleviate premature termination.

4.3. Ablation Studies

We further conduct ablation studies to assess the effectiveness of all components in FARM. Table 5 reports ablations by enabling/disabling SEB, SAB, and RP in different combinations. Because spatial attention relies on channel-wise aggregation and should be applied on well-calibrated channel representations, we do not evaluate the variant swapping the order of SEB and SAB. It is not surprising that the model performs worst when SEB, SAB, and RP are all removed (relying solely on a single convolutional layer Cl_3). Moreover, removing any individual module or pathway also degrades performance comparing to the intact FARM. These results suggest that SEB, SAB, and RP act synergistically, enhancing the capture of subtle anatomical structures while suppressing irrelevant features, thereby improving registration accuracy both individually and holistically.

In addition, we investigate the performance of four TCI configurations on the IXI dataset. Specifically, TCI-1 performs only convergence evaluation, TCI-2 performs only stability evaluation, TCI-3 evaluates convergence before stability, and TCI-4 evaluates stability before convergence (the configuration adopted in iPEAR). Table 6 shows that TCI-4 performs best, showcasing the appropriateness of the proposed TCI design.

Finally, Appendices G~J assess the effectiveness of TCI across different decoding layers and the influence of varying values of thresholds δ_s , δ_c and k_{max} , the choice of similarity metric, and the window size t , respectively.

5. Conclusion

We propose the deformable image registration network iPEAR, which employs FARM to extract anatomical structure details and learn to suppress irrelevant features. Additionally, we introduce the dual-stage TCI strategy to determine the number of optimization iterations. The results

on four datasets demonstrate the effectiveness of iPEAR. Generalizability and ablation studies validate the effectiveness of FARM and TCI. Currently, we combine channel attention and spatial attention to suppress irrelevant features. Going forward, we believe further improvement is achievable by extending this to a multi-head attention mechanism to enhance the model’s capability in feature representation.

References

Avants, B. B., Tustison, N., Song, G., et al. Advanced normalization tools (ants). *Insight J*, 2:1–35, 2009.

Balakrishnan, G., Zhao, A., Sabuncu, M. R., Guttag, J., and Dalca, A. V. An unsupervised learning model for deformable medical image registration. In *Proceedings of IEEE/CVF Conference on Computer Vision and Pattern Recognition*, pp. 9252–9260, 2018.

Balakrishnan, G., Zhao, A., Sabuncu, M. R., Guttag, J., and Dalca, A. V. Voxelmorph: A learning framework for deformable medical image registration. *IEEE Transactions on Medical Imaging*, 38:1788–1800, 2019.

Cai, N., Chen, H., Li, Y., Peng, Y., and Li, J. Adaptive weighting landmark-based group-wise registration on lung DCE-MRI images. *IEEE Transactions on Medical Imaging*, 40:673–687, 2020.

Chen, J., Frey, E. C., He, Y., Segars, W. P., Li, Y., and Du, Y. Transmorph: Transformer for unsupervised medical image registration. *Medical Image Analysis*, 82:102615, 2022.

Cheng, X., Zhang, T., Lu, W., Meng, Q., Frangi, A. F., and Duan, J. SACB-Net: Spatial-awareness convolutions for medical image registration. In *Proceedings of IEEE/CVF Conference on Computer Vision and Pattern Recognition*, pp. 5227–5237, 2025.

De Vos, B. D., Berendsen, F. F., Viergever, M. A., Sokooti, H., Staring, M., and Işgum, I. A deep learning framework for unsupervised affine and deformable image registration. *Medical Image Analysis*, 52:128–143, 2019.

Dice, L. R. Measures of the amount of ecologic association between species. *Ecology*, 26:297–302, 1945.

Fischer, B. and Modersitzki, J. Ill-posed medicine—an introduction to image registration. *Inverse Problems*, 24: 034008, 2008.

Fischl, B. Freesurfer. *Neuroimage*, 62:774–781, 2012.

Hassani, A., Walton, S., Li, J., Li, S., and Shi, H. Neighborhood attention transformer. In *Proceedings of the IEEE/CVF conference on computer vision and pattern recognition*, pp. 6185–6194, 2023.

Hu, B., Zhou, S., Xiong, Z., and Wu, F. Recursive decomposition network for deformable image registration. *IEEE Journal of Biomedical and Health Informatics*, 26: 5130–5141, 2022.

Hu, J., Shen, L., and Sun, G. Squeeze-and-excitation networks. In *Proceedings of IEEE/CVF Conference on Computer Vision and Pattern Recognition*, pp. 7132–7141, 2018.

Hu, Y., Zhao, Z., Zhang, Q., Xu, L. X., and Sun, J. Rdmr: Recursive inference and representation disentanglement for multimodal large deformation registration. In *Proceedings of Medical Image Computing and Computer Assisted Intervention*, pp. 512–522, 2025.

Huttenlocher, D. P., Klanderman, G. A., and Rucklidge, W. J. Comparing images using the hausdorff distance. *IEEE Transactions on Pattern Analysis and Machine Intelligence*, 15:850–863, 1993.

Jaderberg, M., Simonyan, K., Zisserman, A., et al. Spatial transformer networks. volume 28, pp. 2017–2025, 2015.

Kang, M., Hu, X., Huang, W., Scott, M. R., and Reyes, M. Dual-stream pyramid registration network. *Medical Image Analysis*, 78:102379, 2022.

Kingma, D. P. Adam: A method for stochastic optimization. *arXiv preprint arXiv:1412.6980*, 2014.

Klein, A. and Tourville, J. 101 labeled brain images and a consistent human cortical labeling protocol. *Frontiers in neuroscience*, 6:171, 2012.

Li, T., Staring, M., and Qiao, Y. Efficient large-deformation medical image registration via recurrent dynamic correlation. *IEEE Transactions on Medical Imaging (in press)*, 2025.

Liu, Y., Zuo, L., Han, S., Xue, Y., Prince, J. L., and Carass, A. Coordinate translator for learning deformable medical image registration. In *International Workshop on Multi-scale Multimodal Medical Imaging*, pp. 98–109, 2022.

Lv, J., Wang, Z., Shi, H., Zhang, H., Wang, S., Wang, Y., and Li, Q. Joint progressive and coarse-to-fine registration of brain MRI via deformation field integration and non-rigid feature fusion. *IEEE Transactions on Medical Imaging*, 41:2788–2802, 2022.

Ma, J., Zhang, Y., Gu, S., An, X., Wang, Z., Ge, C., Wang, C., Zhang, F., Wang, Y., and Yinan Xu, e. a. Fast and low-GPU-memory abdomen CT organ segmentation: The flare challenge. *Medical Image Analysis*, 82:102616, 2022.

Ma, T., Dai, X., Zhang, S., and Wen, Y. PIViT: Large deformation image registration with pyramid-iterative vision transformer. In *Proceedings of International Conference on Medical Image Computing and Computer Assisted Intervention*, pp. 602–612, 2023.

Ma, T., Zhang, S., Li, J., and Wen, Y. IIRP-Net: Iterative inference residual pyramid network for enhanced image registration. In *Proceedings of the IEEE/CVF Conference on Computer Vision and Pattern Recognition*, pp. 11546–11555, 2024.

Rana, S., Hampson, R., and Dobie, G. Breast cancer: Model reconstruction and image registration from segmented deformed image using visual and force based analysis. *IEEE Transactions on Medical Imaging*, 39:1295–1305, 2019.

Shattuck, D. W., Mirza, M., Adisetiyo, V., Hojatkashani, C., Salamon, G., Narr, K. L., Poldrack, R. A., Bilder, R. M., and Toga, A. W. Construction of a 3D probabilistic atlas of human cortical structures. *Neuroimage*, 39:1064–1080, 2008.

Taha, A. A. and Hanbury, A. Metrics for evaluating 3D medical image segmentation: Analysis, selection, and tool. *BMC Medical Imaging*, 15:1–28, 2015.

Wang, H. and Wang, Y. Equivariance and motion-enhanced neighborhood attention-based pyramid network for 3D deformable medical image registration. *Biomedical Signal Processing and Control*, 108:107897, 2025.

Wang, H., Ni, D., and Wang, Y. Recursive deformable pyramid network for unsupervised medical image registration. *IEEE Transactions on Medical Imaging*, 43:2229–2240, 2024.

Zhao, S., Dong, Y., Chang, E. I., Xu, Y., et al. Recursive cascaded networks for unsupervised medical image registration. In *Proceedings of the IEEE/CVF International Conference on Computer Vision*, pp. 10600–10610, 2019a.

Zhao, S., Lau, T., Luo, J., Chang, E. I.-C., and Xu, Y. Unsupervised 3D end-to-end medical image registration with volume tweening network. *IEEE Journal of Biomedical and Health Informatics*, 24:1394–1404, 2019b.

Zhou, S., Hu, B., Xiong, Z., and Wu, F. Self-distilled hierarchical network for unsupervised deformable image registration. *IEEE Transactions on Medical Imaging*, 42:2162–2175, 2023.

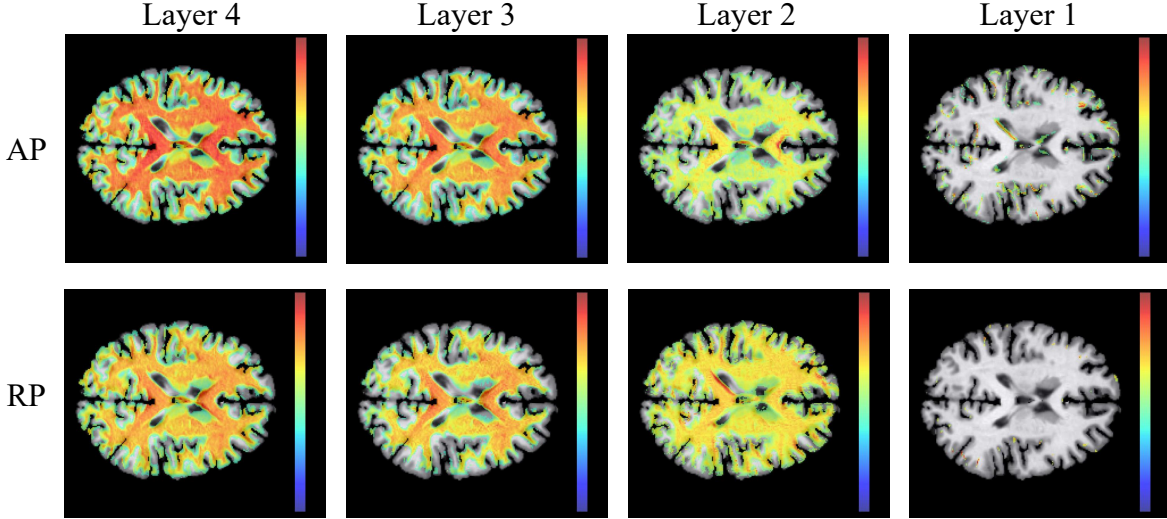


Figure B. Visualization of Feature Attention Patterns for AP and RP.

A. Datasets and Implementation Details

Datasets: Consistent with prior studies (Wang & Wang, 2025; Wang et al., 2024), iPEAR focuses on single-modality registration. Accordingly, to comprehensively assess the performance of the proposed iPEAR, we compare it against different registration models on three public MRI datasets, namely Mindboggle (Klein & Tourville, 2012), LPBA (Shattuck et al., 2008), and IXI (Avants et al., 2009), and one public abdomen CT dataset FLARE (Ma et al., 2022). We preprocess these four datasets as follows. For the Mindboggle dataset, we choose the NKI-RS-22 and NKI-TRT-20 sub-datasets from Mindboggle101 as the training set and OASIS-TRT-20 as the test set, following the prior study (Ma et al., 2024). We crop each volume to $160 \times 192 \times 160$ with an isotropic voxel size of 1 mm, while all images are pre-aligned with the MNI 152 template space. The LPBA dataset contains 40 T1-weighted MRI volumes, each annotated with 54 manually labeled Regions of Interest (ROIs). All volumes have been rigorously pre-aligned to the MNI 305. Specifically, each volume is cropped to $160 \times 192 \times 160$ voxels with an isotropic voxel size of 1 mm. We use 31 volumes for training and 9 for testing, following the prior study (Wang et al., 2024). The IXI dataset contains the original brain MRI images provided by (Fischl, 2012) and their corresponding 3D volume data after affine registration. All volumes are resampled to a voxel size of $80 \times 96 \times 112$ (isotropic voxel size of 2 mm), and for training, we use 407 3D volumes (total 407×406 paired samples), and for testing, 58 volumes (total 58×57 paired samples), following the prior study (Wang et al., 2024). The FLARE dataset consists of 361 scans annotated with four organ labels, namely liver, kidney, spleen, and pancreas. Each volume is cropped to $128 \times 128 \times 96$ voxels with an isotropic voxel size of 2.5 mm. We allocate 341 volumes for training and 20 for testing following the (Ma et al., 2024).

Metrics: To comprehensively assess the performance of various registration models, we adopt multiple quantitative metrics. The Dice score (Dice, 1945) measures region-wise overlap, while the 95% maximum Hausdorff Distance (HD95) (Huttenlocher et al., 1993) and the Average Symmetric Surface Distance (ASSD) (Taha & Hanbury, 2015) quantify the similarity of the regional profiles. The quality of the estimated deformation field φ is assessed by the percentage of voxels with non-positive Jacobian determinant $|J_\varphi| \leq 0$ (i.e., folded voxels). In addition, we report Mean Squared Error (MSE), Inference Time (s), and model size (the number of parameters) for a comprehensive performance analysis.

Implementation Details: Our Model is implemented using Pytorch and trained on an NVIDIA GeForce RTX 4090 GPU. Following the prior study (Ma et al., 2024), we normalize all images to the range $[0, 1]$, optimize using the ADAM optimizer (Kingma, 2014) at a learning rate of 1×10^{-4} , and set the size of volumetric patch n , hyperparameter λ , and batch size to 27, 1, and 1, respectively. In FARM, we adopt a reduction ratio $r = 16$. In TCI, we set stability threshold δ_s , convergence threshold δ_c , the window size t , and the maximum number of iterations k_{max} to 0.005, 0.005, 3, and 10, respectively.

B. Visualization of Feature Attention Patterns for AP and RP

As shown in Figure B, we illustrate the distinct feature attention patterns of AP and RP at each decoding Layer. The AP heatmaps concentrate more strongly on core registration regions (e.g., central gray matter), exhibiting a markedly higher

Table C. Performance comparison of different registration models on the Mindboggle, LPBA, and IXI datasets evaluated by HD95, ASSD, and MSE metrics

Model	Mindboggle			LPBA			IXI			
	HD95 \downarrow	ASSD \downarrow	MSE(10^{-3}) \downarrow	HD95 \downarrow	ASSD \downarrow	MSE(10^{-3}) \downarrow	HD95 \downarrow	ASSD \downarrow	MSE(10^{-3}) \downarrow	
Cascade U-Net	VM (CVPR'18)	5.683	1.726	7.449	6.557	2.089	2.293	1.460	0.584	0.727
	TM (MIA'22)	5.399	1.561	5.500	6.439	1.962	1.179	1.432	0.557	0.432
Pyramid	RCN (ICCV'19)	5.090	1.439	4.607	5.817	1.777	2.005	1.397	0.563	0.518
	SDH-Net (TMI'23)	5.047	1.413	4.616	5.750	1.682	0.963	1.362	0.510	0.392
PiViT (MICCAI'23)	RDN (JBHI'22)	5.041	1.468	5.884	5.817	1.747	1.365	1.270	0.512	0.570
	PR++ (MIA'22)	5.312	1.510	4.871	6.060	1.778	0.852	1.290	0.508	0.360
PiViT (MICCAI'23)	I2G (MMMI'22)	5.129	1.474	4.347	5.646	1.665	1.018	1.301	0.509	0.408
	RDP (TMI'24)	4.992	1.392	4.191	5.618	1.621	0.633	1.229	0.472	0.234
PiViT (MICCAI'23)	IIRP (CVPR'24)	4.947	1.393	4.163	5.737	1.605	0.623	1.225	0.476	0.236
	SACB (CVPR'25)	4.884	1.386	4.852	5.862	1.326	0.837	1.297	0.504	0.351
PiViT (MICCAI'23)	NAP (BSPC'25)	4.832	1.373	4.031	5.570	1.384	0.707	1.228	0.470	0.233
	iPEAR (ours)	4.912	1.366	3.972	5.569	1.652	0.609	1.231	0.460	0.231

response density, whereas the RP responses are more uniformly distributed. In addition, at deep decoder layers (e.g., 4th Layer, corresponding to the coarse registration stage), large global structural discrepancies between the warped and fixed images encourage the network to exploit multi-regional features, resulting in widespread high-response regions in the heatmaps. As decoding proceeds from deep to shallow layers, registration errors decrease and anatomical structures become increasingly aligned, so the model primarily focuses on local regions for fine-grained adjustments. These visualizations demonstrate the rationality of our dual-pathway design.

C. Performance Comparison on HD95, ASSD, and MSE Metrics

In Table C, we present the performance of different registration models on the Mindboggle, LPBA, and IXI datasets, evaluated by the HD95, ASSD, and MSE metrics. The experimental results demonstrate that iPEAR outperforms the other registration models in most scenarios and achieves SOTA results on at least two metrics for each dataset.

D. Visualization of Registration Results on the LPBA Dataset

In Figure D, we present the registration results and corresponding deformation fields across different models on the LPBA dataset. On LPBA, performance differences among models are more noticeable in the structural region of the brain images, highlighted using the blue box. These visualizations further show that, after warping with the deformation fields estimated by iPEAR, the moving images exhibit closer alignment with the fixed images.

E. Quantitative Analysis on Different Anatomical Structures

Following the prior study (Wang et al., 2024), we evaluate iPEAR’s registration performance on selected regions in both hemispheres to assess its accuracy across diverse anatomical structures. Specifically, Figure E.1 presents the Dice scores for seven brain regions in the LPBA dataset, including the frontal, parietal, temporal, occipital, cingulate, hippocampus, and putamen. Figure E.2 presents the Dice scores for seven brain regions in the Mindboggle dataset, including the frontal, parietal, temporal, occipital, third ventricle, fourth ventricle, and brainstem. Figure E.3 presents the Dice score across 30 regions of the IXI dataset. All these experimental results demonstrate that iPEAR outperforms existing registration models.

F. Performance Comparison of Different Iteration Strategies

In this section, we examine the effectiveness of TCI in mitigating premature termination, and report the number of iterations determined by TCI and by the single-stage stopping strategy, respectively. As shown in Table F, on the Mindboggle and FLARE datasets, TCI judiciously increases the average number of iterations across all decoding levels, with the

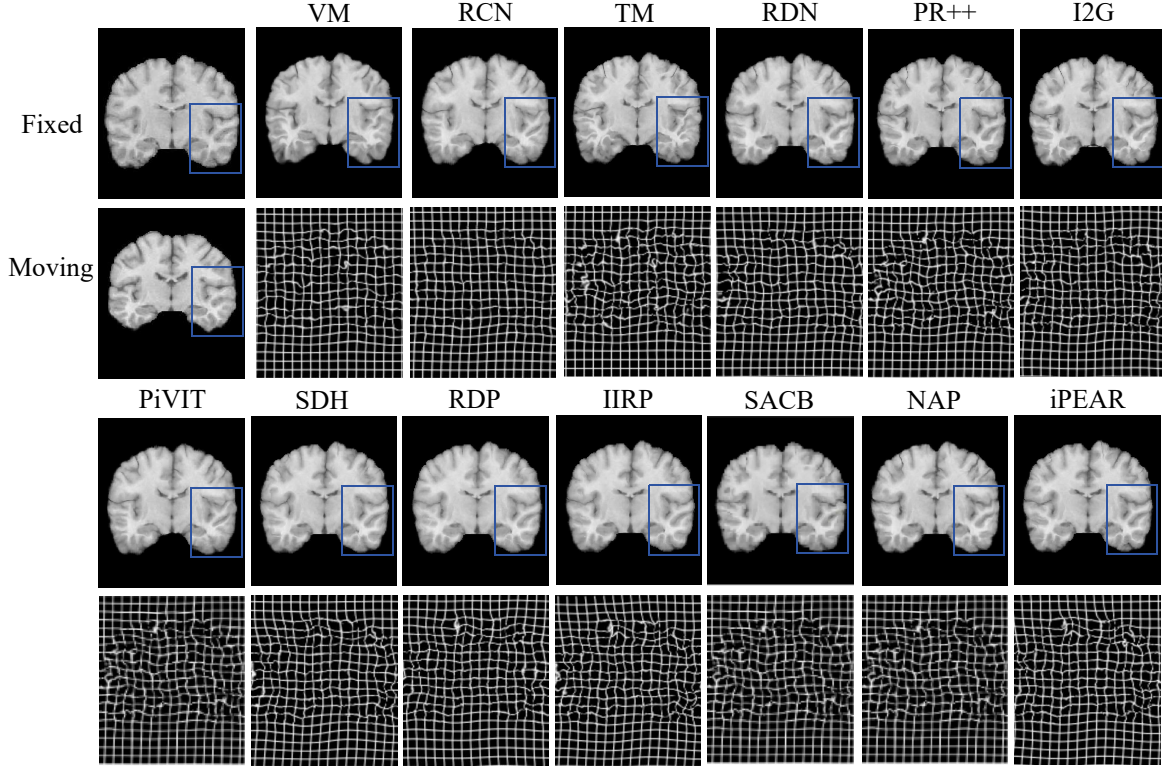


Figure D. Visualization of registration results and corresponding deformation fields across different models on the LPBA dataset.

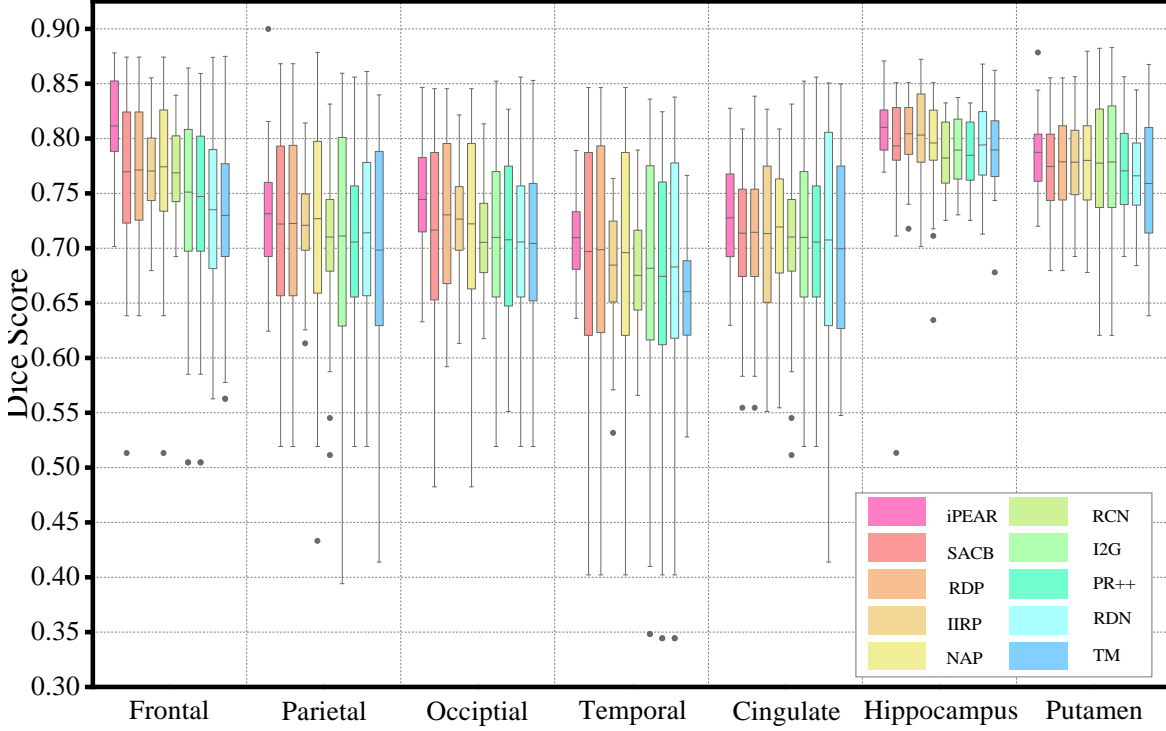


Figure E.1. Performance comparison of different models in seven regions of the LPBA dataset.

largest increase at 4th Layer. The average number of iterations rises from 1.2 to 3.9 and from 1.3 to 3.0 on the two datasets, respectively. This deeper iterative refinement reduces the risk of early-stage under-optimization and helps limit the

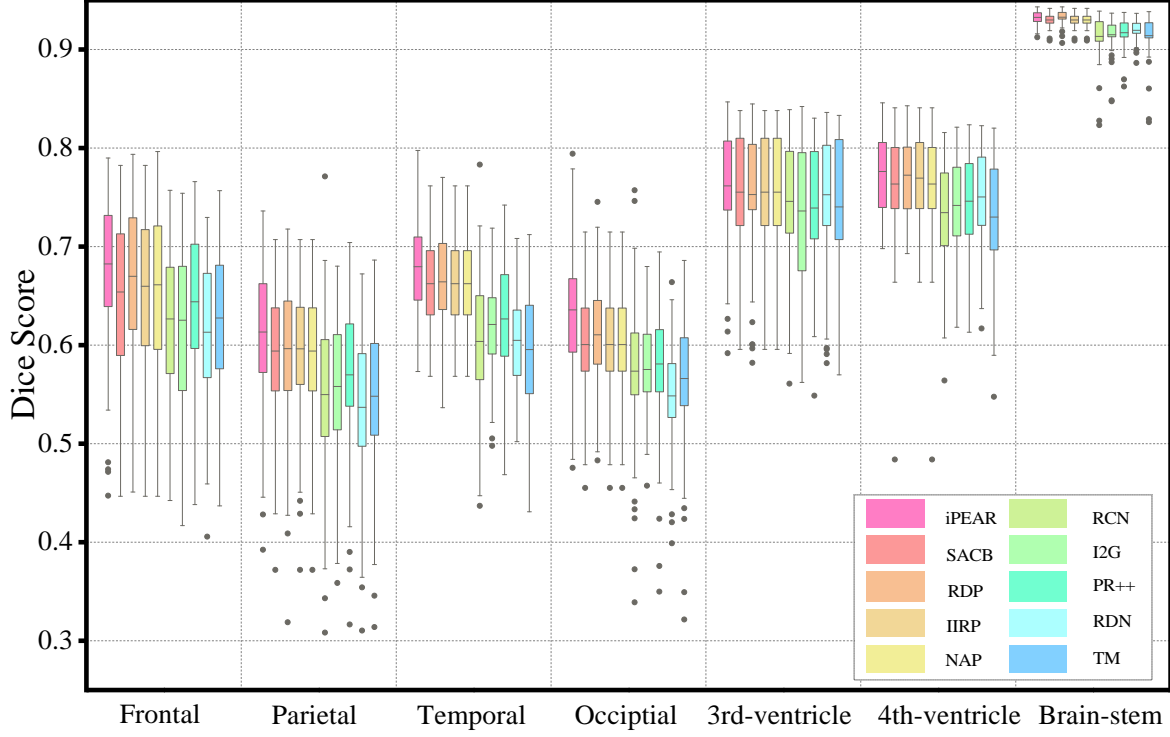


Figure E.2. Performance comparison of different models in seven regions of the Mindboggle dataset.

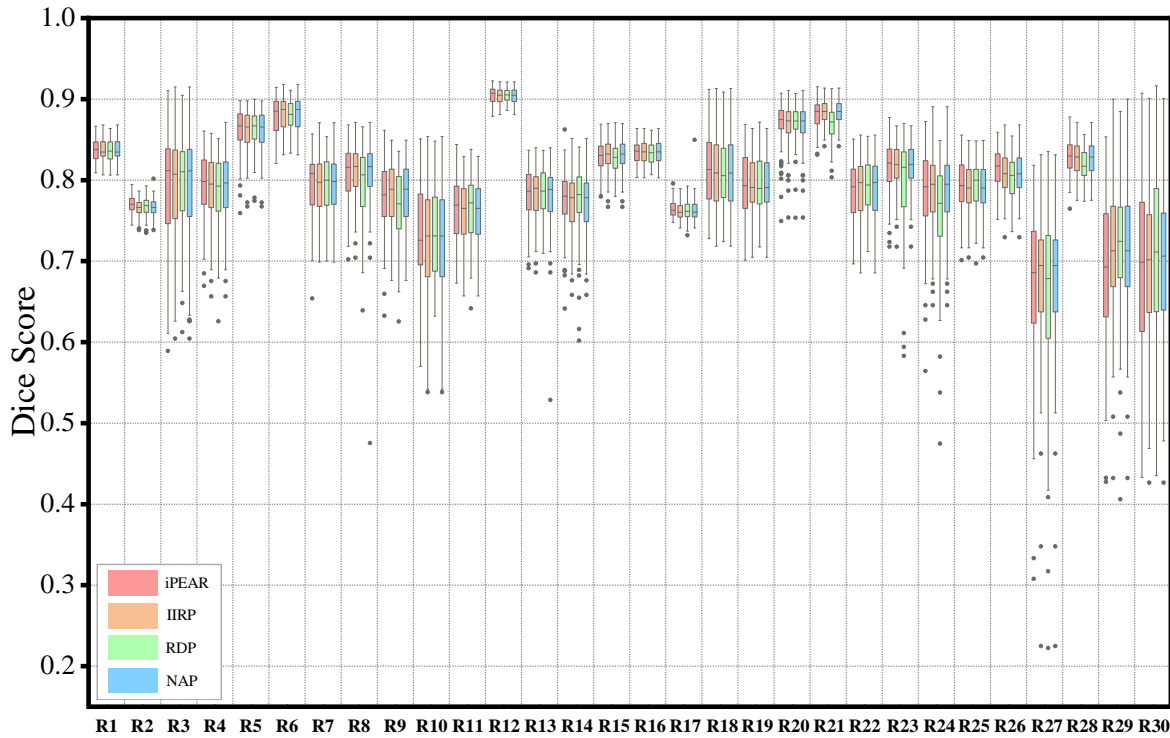


Figure E.3. Performance comparison of different models in thirty regions of the IXI dataset.

accumulation of anatomical misalignments. In addition, we compare TCI with a fixed-iteration setting, and the results show that TCI yields better registration performance than using a fixed number of iterations.

Table F. Performance comparison of different iteration strategies on the Mindboggle and FLARE datasets

	Mindboggle			FLARE		
	Dice(%)↑	MSE(10^{-3})↓	Iter	Dice(%)↑	MSE(10^{-3})↓	Iter
IIRP	65.8	4.16	[1.2, 3.5, 2.0, 2.0]	73.8	3.59	[1.3, 3.4, 3.0, 2.6]
IIRP (Iter = 2)	65.8	4.15	[2.0, 2.0, 2.0, 2.0]	73.6	3.66	[2.0, 2.0, 2.0, 2.0]
IIRP (Iter = 3)	66.0	4.03	[3.0, 3.0, 3.0, 3.0]	74.1	3.50	[3.0, 3.0, 3.0, 3.0]
IIRP (Iter = 4)	65.5	4.49	[4.0, 4.0, 4.0, 4.0]	73.7	3.61	[4.0, 4.0, 4.0, 4.0]
IIRP + TCI	66.2	3.56	[3.9, 3.5, 3.2, 3.0]	74.6	3.40	[3.0, 3.4, 3.6, 3.0]

Table G. Ablation study on the effectiveness of TCI on various decoding layers

Layer 4	Layer 3	Layer 2	Layer 1	Mindboggle	LPBA	IXI
✓				64.9	71.7	79.8
	✓			65.9	72.9	79.7
		✓		65.8	72.7	79.8
			✓	65.8	73.0	79.9
				66.0	73.1	79.9
✓	✓			66.2	73.4	80.0
✓	✓	✓		67.3	73.6	80.2
✓	✓	✓	✓	67.9	73.7	80.6

Table H. Ablation study on thresholds δ_s and δ_c values

δ_s	δ_c	Mindboggle		LPBA		IXI	
		0.01	0.005	0.01	0.005	0.01	0.005
0.01	65.9	66.3	73.1	73.2	80.4	80.4	
0.005	66.8	67.9	73.4	73.7	80.3	80.6	
0.001	67.0	67.6	73.3	73.4	80.3	80.2	

G. Effectiveness of TCI at Each Decoding Layer

In this section, we conduct ablation studies to assess the effectiveness of TCI at each decoding layers. Omitting TCI at a given layer fixes the number of iterations to one, thereby preventing iterative refinement of the deformation field. As shown in Table G, progressively enabling TCI across additional layers steadily improves iPEAR’s performance. Notably, applying TCI at higher-resolution layers (e.g., Layer 1) yields larger performance gains than at lower-resolution layers (e.g., Layer 4). A plausible reason for this is that higher-resolution feature maps more closely match the original image dimensions, preserving fine-grained structural details. Consequently, determining the number of iterations for higher-resolution layers yields greater performance improvements.

H. Impact of Varying Values of Thresholds

In this section, we investigate the sensitivity of the predetermined thresholds δ_s and δ_c . As shown in Table H, these two thresholds exhibit low sensitivity to variation and have minimal impact on the overall performance of iPEAR. Nonetheless, we choose the middle range values, i.e., $\delta_s = 0.005$ and $\delta_c = 0.005$, which yield the best performance.

In addition, in Figure H.1, we present the number of iterations per decoding layer determined by TCI on the IXI dataset. The experimental results demonstrate that three or four iterations suffice for convergence in most cases. Hence, our predefined maximum number of iterations $k_{max} = 10$ is reasonable.

I. Impact of Different TCI Similarity Metrics

In this section, we investigate how three similarity metrics, namely Normalized Cross-Correlation (NCC), Mean Absolute Error (MAE), and Mean Squared Error (MSE), affect the performance of TCI on the IXI dataset. As shown in Table I, NCC delivers the best results. Hence, we adopt NCC as the similarity metric for all experiments in this paper.

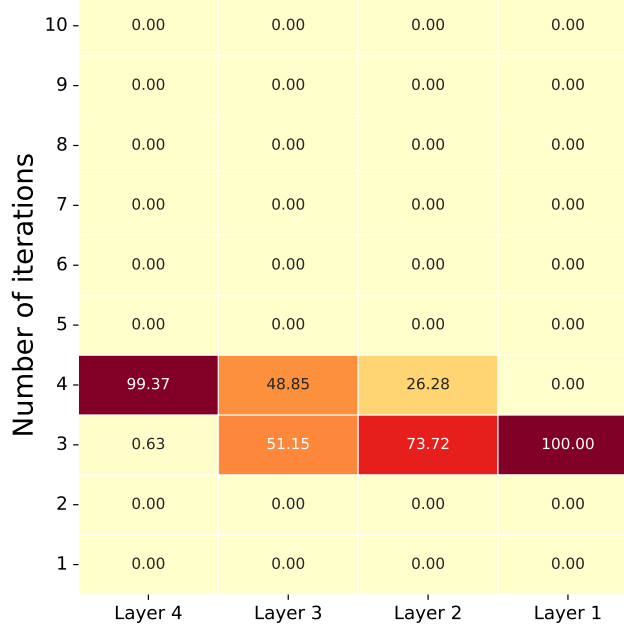


Figure H.1. Statistics of the number of iterations across different decoding layers.

Table I. Ablation study on the effectiveness of different similarity metrics adopted in TCI

$\delta_s \backslash \delta_c$	MAE		MSE		NCC	
	0.01	0.005	0.01	0.005	0.01	0.005
0.01	79.6	79.7	80.0	79.5	80.4	80.6
0.005	79.7	80.0	79.9	80.1	80.6	80.6
0.001	80.2	79.1	80.1	79.9	80.4	80.2

Table J. Ablation study on the different window sizes

t	IXI					Mindboggle				
	Dice(%) \uparrow	HD95 \downarrow	ASSD \downarrow	MSE(10^{-3}) \downarrow	Time(s) \downarrow	Dice(%) \uparrow	HD95 \downarrow	ASSD \downarrow	MSE(10^{-3}) \downarrow	Time(s) \downarrow
3	80.6	1.23	0.46	0.23	0.12	67.9	4.91	1.37	3.97	0.19
4	80.9	1.22	0.46	0.21	0.15	67.4	4.93	1.38	3.89	0.22
5	80.7	1.27	0.49	0.23	0.29	67.0	4.94	1.39	4.06	0.35

J. Impact of Different Sliding Window Sizes

In Table J, we present the effect of window size t on the performance of iPEAR. On the IXI dataset, increasing t from 3 to 4 yields marginal performance gains but incurs longer inference time. Increasing t further to 5 degrades performance across all metrics, suggesting that $t = 4$ provides sufficient iterative refinement without incurring excessive iterations. On the Mindboggle dataset, setting $t = 3$ outperforms $t = 4$ on most metrics, likely because $t = 4$ induces excessive iterations in TCI's deformation refinement. Therefore, we set $t = 3$ for all experiments in this paper.